Graphical Abstract

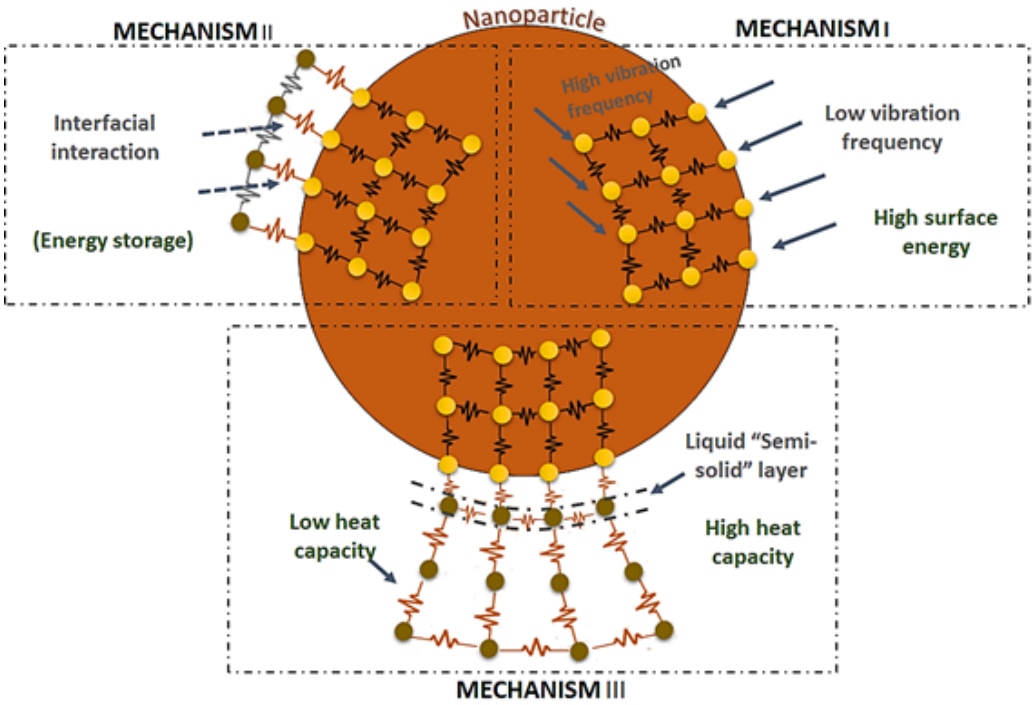

Three mechanisms have been proposed as candidates to explain the unconventional C_p increment phenomenon in nanofluids. Adapted from Ref. (6). Mechanism I: The superficial atoms of the nanoparticles are less limited since they have a smaller number of bonds. Therefore, this superficial atom oscillates at lower natural frequencies and high amplitudes, resulting in a higher superficial energy. Mechanism II: The interaction of nanoparticle's surface atoms with the ionic salt. Mechanism III: The presence of a semi-solid layer around the nanoparticles surface contributes to the C_p increment of the nanofluid.

Effect of nanoparticles in molten salts – MD simulations and experimental study

Adela Svobodova-Sedlackova[1], Camila Barreneche[1], Gerard Alonso[1,2], A. Inés Fernandez[1*], Pablo Gamallo[1,2*]

[1]*Departament de Ciència de Materials i Química Física, Universitat de Barcelona, C/Martí i Franqués 1, 08028, Barcelona, Spain.*
[2]*Institut de Química Teòrica i Computacional, IQTC-UB, Universitat de Barcelona, C/Martí i Franqués 1, 08028, Barcelona, Spain.*
***Corresponding author's e-mail: ana_inesfernandez@ub.edu**

Abstract

Highlighted experimental studies on nanofluids reveal an anomalous increment in the specific heat capacity (C_p) of these ionic systems when nanoparticles are added. This fact is really important due the applicability of nanofluids in concentrating solar power plants as heat transfer fluid and storage media. These are promising results for the development of high-temperature heat storage applications by enhanced storage capacity materials. The present work focuses on the study of this effect in $NaNO_3$ molten salt doped with SiO_2 nanoparticles by molecular dynamics (MD) simulations and Differential Scanning Calorimetry (DSC) experiments. The study shows that for nanoparticles' concentrations around 1% wt. the C_p increases by 26% compared to pure $NaNO_3$, whereas at higher concentrations the effect disappears. The results approach high agreement between experimental and simulation results and MD simulations reveal that the increase of C_p at low concentrations is explained by the formation of a semi ordered layer of ionic fluid. This layer is rich in Na^+ cations, around the nanoparticles whereas the reduction of C_p at concentrations higher than 2% wt. is related to the aggregation of nanoparticles as revealed by Scanning Electron Microscopy (SEM). However, deep experimental results with other materials will be required in order to validate the layering effect.

Keywords: Nanofluids; molten salt; silica nanoparticles; concentrating solar power CSP; solar energy; simulations.

1. Introduction

Development, research and innovation in energy storage systems are indispensable for an energy transition to low carbon technologies, because they allow the full penetration of renewable energies in our energy system. Solar energy sources play an important role in the energy field, due to the great uncertainty over future energy supplies and to environmental issues. Concentrated solar power (CSP) plants are becoming one of the most massively implemented cost-efficient solar technology. The global world CSP capacity forecast to hit 10-22 GW by 2025. Thereby, all new CSP facilities that come online incorporate Thermal Storage (TES) systems. The main purpose of the thermal storage system is to mitigate renewable energy intermittency, to extend the power production period and to prevent possible black-outs of the CSP plant[1]. TES used in CSP[2] plants store energy as sensible heat. For this purpose, molten salts are used as thermal energy storage medium or heat transfer fluid (HTF). The eutectic mixture of 60% sodium nitrate and 40% potassium nitrate known as Solar Salt[3], shows better thermal properties and a lower cost than mineral oils used as HTF. However, the main disadvantages are the low specific heat capacity (i.e., C_p~2 $Jg^{-1}K^{-1}$) and corrosion issues that may hinder the storage[4] .

TES materials with enhanced thermal properties (e.g., high thermal stability and high C_p) are required to achieve high-energy efficiency in the CSP, since these materials could increase the operating range of the storage facilities, reduce the volume of storage tanks[1,5], and decrease the cost of solar power technology to compete with coal fired power plants in the near future[6]. Recent studies show that molten salts doped with low concentrations of nanoparticles produces a nanofluid with an unconventional C_p increment[7,8]. For these reasons, more investigations in the last years are focused on improving this key parameter and studying these nanofluids[9,10,11,12,13,14,15]. Most studied nanofluids showing this behavior are composed by silica, alumina or copper oxide nanoparticles[16,17,18,19,20,21]. However, despite the C_p increment phenomenon observed in all these studies, there are great discrepancies among all of them, not

only because of the different experimental conditions reported in the studies but also for the different theoretical models that could explain the effect[22,23]. Nowadays, there are three proposed mechanisms to explain that increment of C_p (Figure 1). The first mechanism proposes that nanoparticles increase C_p due to the high surface energy per nanoparticle unit mass[24]. In fact, Lan et al.[25] argue through a theoretical model that a decrease of the nanoparticle size increases the C_p being a function of the nanoparticle's nominal diameter. The second mechanism suggests that the particle-liquid interface has an anomalous high resistance[24,26] which acts as a mechanism of thermal energy storage. Finally, the third mechanism considers the formation of a semi-solid structured layer (i.e., nano-layering) around the nanoparticles[27]. Although the C_p value for solids is commonly lower than for liquids, the presence of this semi-solid layer could enhance the C_p value of the nanofluid.

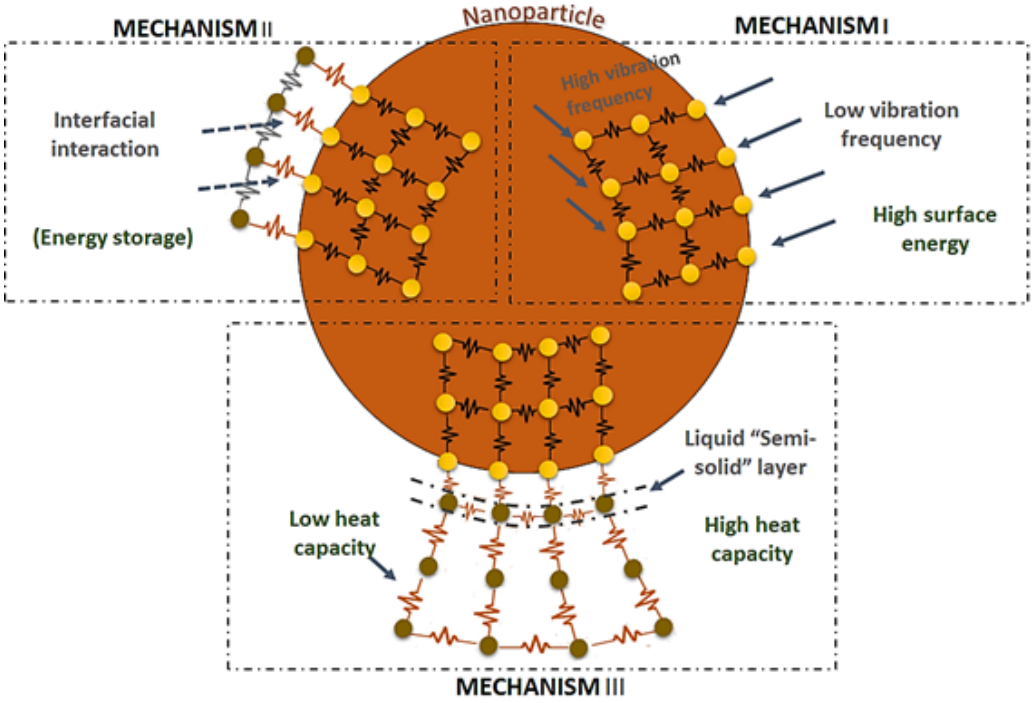

Figure 1. Three proposed mechanisms as candidates to explain the unconventional C_p increment phenomenon in nanofluids. Adapted from Shin et al.[6]

The two former mechanisms increase C_p since they increase the degrees of freedom of the system. However, mechanism three is not yet confirmed. The main scope of this paper is

to understand the unconventional C_p increment. If this phenomenon is controlled, the use of nanofluids as HTF and TES media in CSP will mark a turning point in this technology. Therefore, the TES system, for example, will be more compacted and more efficient from an energetic point of view.

Therefore, the present study is focused on the effect in C_p values of the concentration and the size of silica nanoparticles in molten sodium nitrate salt. The computational and experimental results obtained aims to clarify the inconsistency and high variety of results reported in the literature and to find clear trends about the mechanisms that govern the C_p increase in nanofluids.

2. Methodology, systems and validation

2.1. Molecular dynamic simulations

Molecular Dynamics (MD) simulations were carried out with Large-scale Atomic/Molecular Massively Parallel Simulator (LAMMPS) code[28]. The trajectory of each particle is obtained by integration of Newton's equations of motion with a 1 fs timestep, during 10^5 time steps for equilibration, and 10^5 time steps for production. The equilibration was performed in three consecutive steps: i) a thermal ramp to raise the temperature up to 773 K with the Langevin thermostat[29] (without barostat), ii) a thermal equilibration phase at the desired temperature with the same thermostat and iii) a pressure equilibration phase, with the Berendsen barostat[30] to achieve the pressure of 1 atm keeping the temperature constant. Once the equilibrium was reached, the system was time evolved with the isothermal-isobaric ensemble (NPT) using the Nosé-Hoover thermostat and barostat[31,32] with 0.1 ps and 1 ps of relaxation time, respectively.

Equation (1) describes the energy of the system, U_{pot}, that is calculated as a sum of internal or bonded terms, U_{bonded}, which describe the bonds, angles and rotations in a molecule

and a sum of external or non-bonded terms, $U_{non-bonded}$, that account for interactions between non-bonded atoms.

$$U_{pot} = U_{bonded} + U_{non-bonded} \quad (1)$$

Thus, the bonded terms in Equation (2) represents the harmonic potentials shown in Equation (3-5),

$$U_{bonded} = U_{bond-stretch} + U_{angle-bending} + U_{improper} \quad (2)$$

$$U_{bond-stretch} = \sum_{\substack{1,2pairs \\ i,j}} K_b^{ij} (b - b_0)^2 \quad (3)$$

$$U_{angle-bending} = \sum_{angles} K_\theta \ (\theta - \theta_0)^2 \quad (4)$$

$$U_{improper} = \sum_{improper} K_{imp} (\psi - \psi_0)^2 \quad (5)$$

where the former is the approximation to the energy of a bond as a function of the displacement from the ideal bon length, b_0, and the force constant, K_b^{ij}, determines the strength of the bond. Both, ideal bond lengths and force constants are specific for each pair of bound atoms. The same kind of functions are used to describe the bending of an angle around its equilibrium value, θ_0, and so on.

Equation (6) describes the non-bonded or intermolecular interactions. They were calculated using a Buckingham potential[33], Equation (7), for dispersion forces and a Coulomb potential[34], Equation (8), for electrostatic interactions.

$$U_{non-bonded} = U_{Buckingham} + U_{Coulomb} \quad (6)$$

$$U_{Buckingham} = \sum_i \sum_{j \neq i} A_{ij} e^{-r_{ij}/\rho_{ij}} - \frac{C_{ij}}{r_{ij}^6} \quad r_{ij} < r_c \quad (7)$$

$$U_{Coulomb} = \sum_i \sum_{j \neq i} \frac{q_i q_j}{\varepsilon r_{ij}} \quad r_{ij} < r_c \quad (8)$$

where r_{ij} is the intermolecular distance, q_i, is the charge of i-species, r_c the cutoff distance and ρ_{ij}, A_{ij} and C_{ij}, are the force field corresponding parameters. Here, the dielectric function, ε, in Equation (8) is set to one since the solvent is treated explicitly in the simulations. The cutoff for both potentials was set to 11 Å and long-range interactions were accounted: i) with analytic tail corrections for the Buckingham potential, and ii) with the Particle-Particle/Particle-Mesh for the Coulomb potential.

The force field parameters to reproduce $NaNO_3$ were obtained from Jayaraman et al.,[35] and the silica parameters were taken from Qiao and Emami et al.[24,36] $NaNO_3$ species were considered a flexible group and its intramolecular parameters (i.e., the N-O bond, the O-N-O angle and the O-N-O-O improper angle) are listed in Table 1, along with the whole set of intermolecular parameters. Otherwise, the silica nanoparticle was simulated as both rigid and flexible body to evaluate the effect of the vibration of nanoparticles in the calculation of nanofluids properties.

Table 1. Force Field parameters for $NaNO_3$ and SiO_2 nanoparticles.

Non-bonding parameters				
atom	q_i **(e)**	A_{ii} **(kcal/mol)**[a]	ρ_{ii} **(Å)**	C_{ii} **(kcal/mol·Å^6)**
Na	1	9778.060	0.3170	24.18
N	+0.95	33652.750	0.2646	259.10
O (in $NaNO_3$)	-0.65	62142.900	0.2392	259.40
O (in SiO_2)	-0.955209	15170.700	0.3860	617.24
Si	1.910418	72460.640	0.3510	14415.29
H	+ 0.4776	7194.197	0.2500	0
Bonding parameters				
N-O	K_b^{NO} = 525.0 kcal·mol^{-1}·Å^{-2}		b_0 = 1.2676 Å	
O-N-O	K_θ = 105.0 kcal·mol^{-1}·rad^{-2}		θ_0 = 120.0°	
O-N-O-O	K_{imp} = 60.0 kcal·mol^{-1}·rad^{-2}		ψ_0 = 0.0°	
Si-O	K_b^{SiO} = 285.0 kcal·mol^{-1}·Å^{-2}		b_0 = 1.680 Å	
O-H	K_b^{OH} = 495.0 kcal·mol^{-1}·Å^{-2}		b_0 = 0.945 Å	
O-Si-O	K_θ = 100.0 kcal·mol^{-1}·rad^{-2}		θ_0 = 109.5°	
Si-O-Si	K_θ = 100.0 kcal·mol^{-1}·rad^{-2}		θ_0 = 149.0°	
Si-O-H	K_θ = 50.0 kcal·mol^{-1}·rad^{-2}		θ_0 = 115.0°	

[a]in the Buckingham potential the crossed terms are calculated as: $A_{ij}=(A_{ii}A_{jj})^{1/2}$, $C_{ij} = (C_{ii}C_{jj})^{1/2}$ and $1/\rho_{ij}=1/\rho_{ii}+1/\rho_{jj}$.

Two different simulation cells were built in this work from the $NaNO_3$ conventional cell obtained from Jayaraman et al.,[35] with dimensions 5.07 Å x 8.78 Å x 16.82 Å and 12 $NaNO_3$ units. The first one, did not contain any nanoparticle and it was created through a (6 x 4 x 2) replication of the conventional cell to obtain 576 $NaNO_3$ units in a box of 30.42 Å x 35.13 Å x 33.64 Å. This cell was used to obtain the heat capacity (C_p), density and crystallographic parameters of the pure $NaNO_3$ which were in good agreement with previous theoretical and experimental values reported in the literature[37,38,12,39,40,41] . The second one was a (18 x 12 x 6) replication of the conventional cell to obtain 15552 $NaNO_3$ units in a box of 91.26 Å x 105.38 Å x 100.93 Å, and it was large enough to contain different nanoparticle concentrations. Nanoparticles of different radii (i.e., from 5 Å to 15 Å) where added as follows: i) nanoparticles were created performing a spherical cut from the bulk structure of SiO_2 (α-quartz) and saturating

the dangling oxygen atoms with hydrogen atoms; ii) nanoparticles are introduced in the simulation cell by deleting the $NaNO_3$ species inside spherical regions with radiuses similar to the nanoparticle radius; and iii) N nanoparticles were added in the N empty regions generated in the previous step.

The heat capacity (C_p) was obtained from MD simulations through the variation of enthalpy with temperature, Equation (9). To that end, different simulations ranging from 598 K to 773 K were performed to obtain the slope of the $\partial H/\partial T$ curve at the pressure of 1 atm. Also, the enthalpy was obtained directly with MD through Equation (10).

$$C_p = \left(\frac{\partial H}{\partial T}\right)_P \tag{9}$$

$$H = U + PV \tag{10}$$

2.2. Nanofluids synthesis

$NaNO_3$ used to manufacture the nanofluids was Sigma Aldrich, 99.995% and spherical silica nanoparticles of 5-15 nm of diameter (Sigma Aldrich, 99.5%). The synthesis of the nanofluids was carried out through the following steps (see Figure 2):

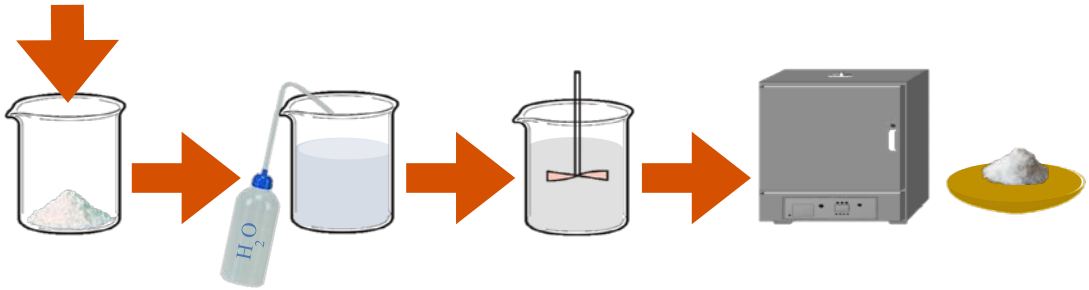

Figure 2. 1-step Nanofluid synthesis scheme.

i) preparation of 40 gr of sample of sodium nitrate + nanoparticles with the respective percentage (w/w) of nanoparticles.

ii) solvation in 30 ml of distilled water.

iii) sonication during 6 minutes for a correct dispersion and homogenization of nanoparticles inside the salt.

iv) drying in an oven at 105º C until complete water evaporation and recrystallization of the material and,

v) sampling and grinding in an Agatha mortar.

For the study of the concentration effect of nanoparticles in the system, $NaNO_3$ samples with [0.5 - 5] % wt. concentration of nanoparticles were prepared.

2.3. Nanofluids characterization

To observe the nanofluids morphology at solid state, the samples under study were characterized using a Scanning Electron Microscopy (ESEM Quanta 200 FEI) at 20 kW. The samples were coated with graphite and the measurements were performed in solid state under vacuum conditions.

X-Ray Powder Diffraction (Panalytical PRO MRD) was employed for the structural characterization. The measurements were performed in transmission geometry, with Cu Kα radiation (λ = 1.5418 Å) and work power of 5 kV – 40 mA, in a main angular range from 4 to 88 º(2θ) with a time step size of 0.026 º(2θ) and a measuring time of 148 seconds per step. Previously, the sample were ground in an Agatha mortar, and sandwiched between low transmission (polyester) films of 3.6 µm of thickness.

The C_p values were measured at 500 ºC with the Differential Scanning Calorimetry from DSC 822e de Mettler Toledo with 50 mL/min of N_2 flow, using the methodology of the areas described by Ferrer et al.[42] A quartering method was employed to obtain representative samples. The amount of sample analyzed in a single experiment was around 10 mg within a 40µl aluminum crucible. For each concentration of nanoparticles, three samples were analyzed to get an averaged C_p value with standard deviation of ±2%.

3. Results and discussion

There are several studies that analyze different effects of introducing nanoparticles in molten salts (*e.g.*, nanoparticle's size, shape, material composition and concentration)[7,12,43,44,45]. However, these studies report results that show a strong inconsistence among them. In general, most of these studies show the biggest increment in C_p when the concentration of nanoparticles is close to 1% wt., but with different sizes of nanoparticles, shapes and composition[46,13,38], indicating that the increase of C_p is inherent to the presence of nanoparticles in the molten salt base fluid and it is not due to the nanoparticles' nature. At the same time, some studies showed that the C_p improves with the size increment[16] while other studies observed the opposite[13]. Moreover, experiments at the same conditions[6,38], showed different C_p increments. These differences can be understood considering the extremely difficult task of sampling in nanofluids and obtaining a good nanoparticle dispersion. On top of that, even computational studies using the same force field parameters[24,12] lead to different C_p values. Therefore, it is clear that these differences observed put some controversy about the thermal storage capacity of the nanofluids.

According to this, the present work is focused on comparing thermal capacities of $NaNO_3$ based nanofluids obtained by using Molecular Dynamics (MD) simulations and Differential Scanning Calorimetry (DSC) experiments. MD simulations have been carried out by means of LAMMPS code[28] with the force field and details previously described in the Methodology section. Just to remark, the force field used has been validated by calculating densities, cell parameters and heat capacities for $NaNO_3$ obtaining an agreement within 10% between experimental and theoretical values[39,40,41,35,47].

3.1. Thermophysical properties

In the MD study, spherical SiO_2 (α-quartz) nanoparticles of 1 nm of diameter are incorporated to $NaNO_3$ at different concentrations, [0 - 10 %] wt. Figure 3 shows the change in

C_p as a function of the nanoparticles concentration until 5% since at higher concentrations C_p values are similar to those of 5%.

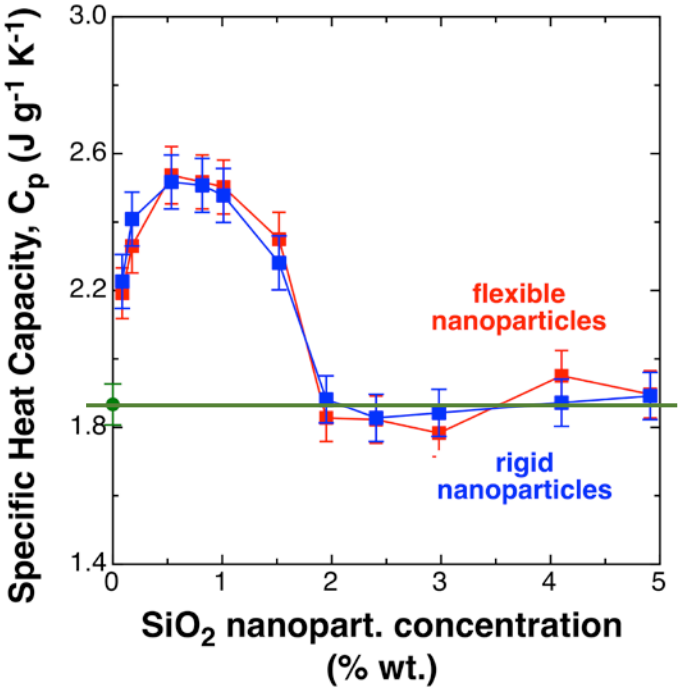

Figure 3. Simulated specific heat capacities for pure $NaNO_3$ (●), and for $NaNO_3$ dispersions of SiO_2 nanoparticles of 1nm (■) of diameter at different concentrations and at 773 K of temperature and 1 atm of pressure. Blue color stands for simulations performed considering nanoparticles as rigid entities (atoms kept fixed) whereas red color stands for nanoparticles where atoms are allowed to move during the simulations.

In a first stage, C_p increases until reaching a top value at 0.5% wt. of nanoparticles. Then, increasing the number of nanoparticles in the medium makes that the C_p value diminishes until recovering the pure $NaNO_3$ value. It is evident that the increase of C_p is only observed at a tiny interval of concentration of nanoparticles, losing the thermal effect as the number of nanoparticles increase within the fluid. The MD simulations have been carried out in two modes with or without freezing the atoms that form the nanoparticles (i.e., considering the nanoparticles as rigid or flexible bodies, respectively). As it is shown in Figure 3, the small difference observed in simulated C_p results for flexible and rigid nanoparticles requires that C_p does not depend on the stiffness or flexibility of the nanoparticles. This fact points out that the shape or nature of the nanoparticles inside the fluid is not so important as suggested by Wang[48].

Nanofluids with more than 2 % wt. nanoparticles exhibit a C_p fall even below the $NaNO_3$ bulk value but these results can be understood taking into account the associated errors in the measure.

Experimentally, samples with different concentrations of SiO_2 of 5-15 nm diameters were studied by DSC. As above-mentioned, the C_p values were determined using the method of the areas of Ferrer et al.[42] Considering the results plotted in Figure 4, there is a proper consistency between experimental and computational increments. Indeed, there is a maximum C_p value, around the 1% wt. of nanoparticles concentration, which qualitatively agrees with MD values. The greatest value observed was ΔC_p = 29 J g^{-1} K^{-1} ± 2 % respect to the $NaNO_3$ bulk value, comparable with the maximum increment obtained through MD simulations ΔC_p = 26 J g^{-1} K^{-1} ± 2 %. These values are far from the hypothetical one coming from the law of mixtures described in Equation (11),

$$C_p = \frac{m_p C_{p,p} + m_f C_{p,f}}{m_p + m_f} \quad (11)$$

where m_p is the nanoparticle mass, m_f is the fluid mass and the $C_{p,p}$ and $C_{p,f}$ are the specific heat capacity of both nanoparticles and the fluid, respectively. Since specific heat capacities of α-quartz and pure $NaNO_3$ are 1.1 $J \cdot g^{-1} \cdot K^{-1}$ and 1.8 $J \cdot g^{-1} \cdot K^{-1}$ at 773 K respectively, the C_p value for the nanofluid is expected to be lower.

According to Figure 4, extraordinary C_p values are obtained for nanoparticles concentrations below 2% wt. both computationally and experimentally. At higher concentrations, this effect is reversed until reaching the constant value predicted by Equation (11). Besides, to validate the tendency between the simulations (with nanoparticles of 1 nm) and the experimental values (with nanoparticles of 5-15 nm), simulations with flexible nanoparticles of 3 nm of nominal diameter were also performed at some concentrations. The obtained values show the same trend obtained for smaller nanoparticles (e.g., ΔC_p (%) = 26, 32 at 0.5% wt. with nanoparticles of 1 nm and 3 nm, respectively, and ΔC_p (%) = 26, 31 at 1% wt.) ensuring the

validity of the results with the size of the nanoparticles. Therefore, even with the smallest nanoparticles simulated, the main trend of anomalous C_p increase is still captured by both methods (i.e., DSC and MD).

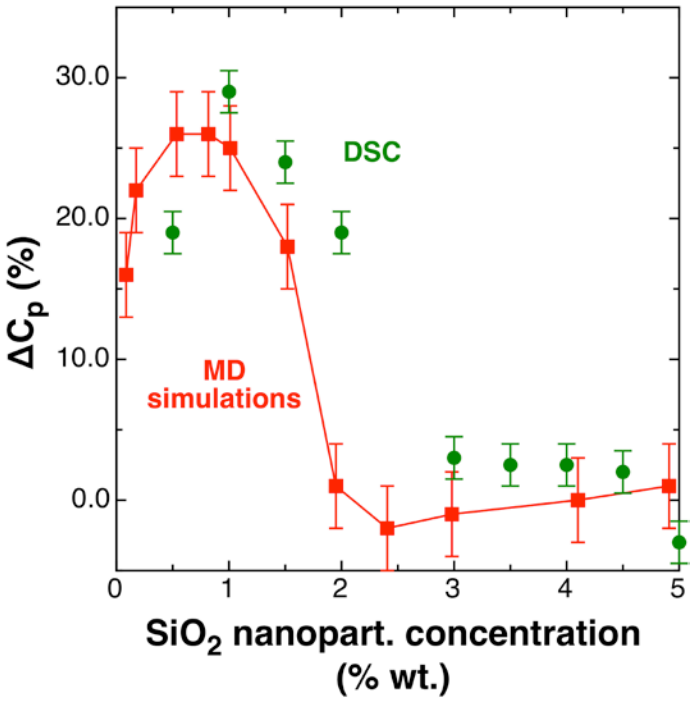

Figure 4. Experimental DSC (●) and MD (■) ΔC_p for $NaNO_3$ + SiO_2 nanofluids as a function of the nanoparticle concentration and at 773 K and 1 atm. Flexible nanoparticles of 1 nm have been used in MD simulations and in the range of 5-15 nm in experimental samples.

It is remarkable that DSC results depend strongly on some experimental parameters that must be controlled during the measurements. These are the mass analyzed, the heating rate, the temperature conditions to perform the analyses, and the sampling in order to ensure a homogenous material to be analyzed (i.e., the same nanoparticle amount over the samples under study of each percentage). As previously commented, temperature is also a key factor to consider during the experiments because the nitrate decomposition. In the present study, the presence of nitrates has been scarce as determined by the UV-visible spectrum of the samples of the nanofluid after the thermal treatment. Thus, the low presence of nitrites during the experimental procedure validates using a non-reactive force field to describe the nanofluid during the simulations.

313 Once the experimental and the simulated C_p values agree, the analysis of MD
314 simulations along with the use of other characterization techniques can help us to distinguish
315 the proposed mechanisms that describe the increase in C_p as a function of nanoparticles
316 concentration.

317 **3.2. Structural Characterization**

318

319 Scanning electron microscopy (SEM) has been used to observe the samples under
320 study. Figure 5 shows several SEM images at different magnitudes and different nanoparticle
321 concentrations.

322

323 As observed, the decreasing of C_p as the nanoparticle concentration increases is
324 related to the agglomeration of the nanoparticles and the loose of effective area when
325 nanoparticles become bigger. Some authors[17] reported the formation of substructures in the
326 nanofluids, and they attributed the unconventional C_p increment phenomenon to these
327 structures, to their high superficial energy, and the formation of agglomeration groups.
328 Furthermore, other authors observed star like structures around the nanoparticles via SEM
329 techniques[18,19]. According to SEM pictures shown in Figure 5, agglomeration of nanoparticles
330 in the $NaNO_3$ becomes more intense at higher concentrations. This process is easily observed in
331 Figure 5.e) where the nanoparticle dispersion is reached and Figure 5.f) where the nanoparticles
332 are highly agglomerated. Due to the presence of agglomeration of nanoparticles at higher
333 concentrations it is expected the existence of a limiting diameter value of nanoparticle from
334 which the thermal capacity effect disappears at all concentrations.

335

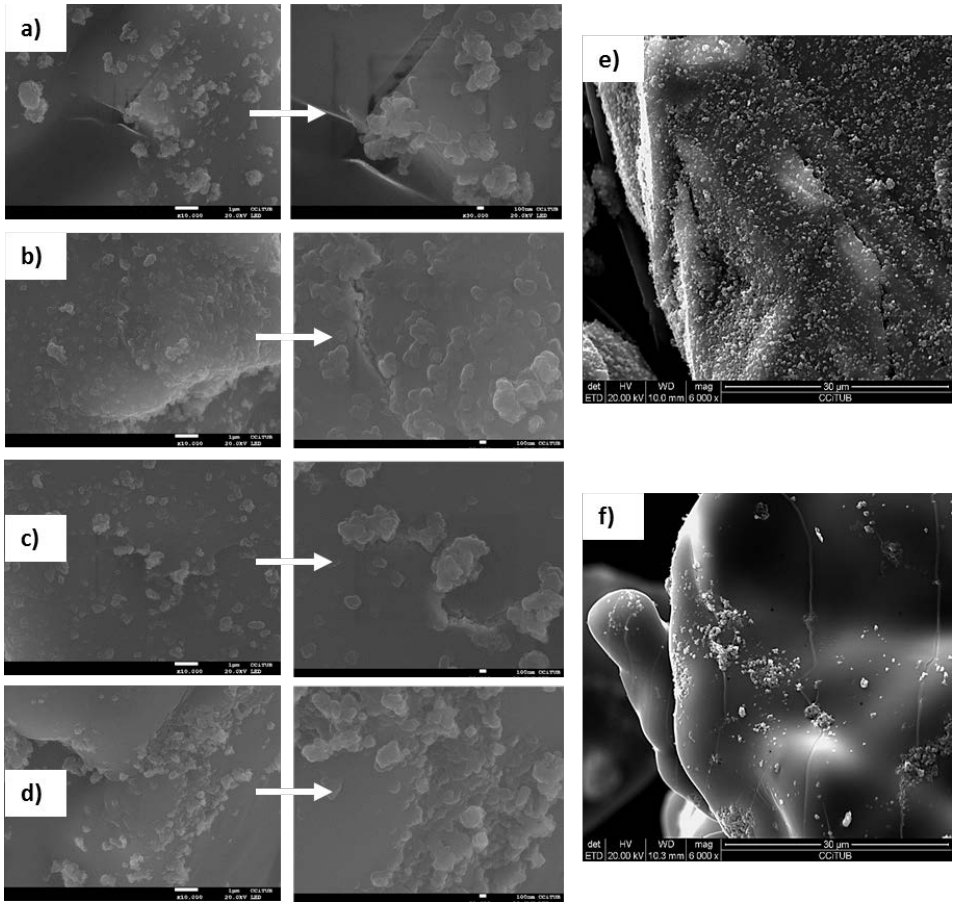

Figure 5. Nanofluids SEM images at different concentrations of nanoparticles at 25ºC (left: x10.000 and right: x30.000): a) 1% wt. SiO_2; b) 2.5% wt. SiO_2; c) 5% wt. SiO_2; and d) 10% wt. SiO_2; e) nanoparticles dispersed in the salt surface, 5% wt. SiO_2, x6.000; f) nanoparticles agglomeration in the salt surface, 10% wt. SiO_2, x6.000.

The main parameters that affect the C_p unconventional values based on the concentration changes and the nanoparticles size within the nanofluids are schematically described in Figure 6.

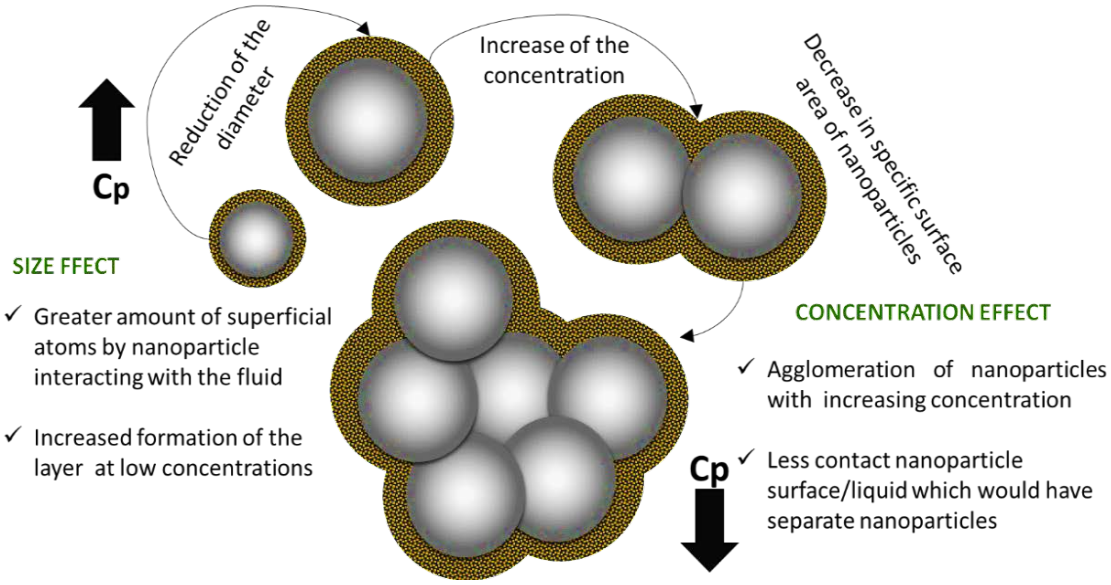

Figure 6. Scheme of the main parameters that affect the C_p. Effect of the concentrations and the size of the nanoparticles in the nanofluids.

In addition, the microstructure has been also studied via X-Ray Powder Diffraction (XRD), to see a possible structural change in the synthetized nanofluids. To do this, new formulations of nanoparticles and $NaNO_3$ samples were prepared at the same nanoparticle concentration in order to analyze how these nanoparticles behave when $NaNO_3$ recrystallizes. The new formulation consists in a physical mixture. The samples were milled in an Agatha mortar and placed between low absorption 3.6 μm films. Then, these samples were measured in transmission geometry. The diagrams obtained are shown in Figure 7 where it is represented the main angular range between 10 to 35, 2θ(°) of the $NaNO_3$ and silica nanoparticles (top) and the two formulations (i.e., namely mixture and synthesized, middle and bottom, respectively) containing 1%, 5% and 10% wt. of nanoparticles. The X-Ray powder diffraction diagrams showed that the higher the nanoparticle concentration, the higher the presence of amorphous signal of the nanoparticles in both types of preparations. Nevertheless, when comparing the two methods, there are significant differences between them. In the case of the synthetized nanofluids, the amorphous phase has less presence than in the others. Therefore, in the case of the synthetized sample containing 1% wt. nanoparticles is not possible to identify the amorphous phase and it exhibits an almost identical diagram than the pure $NaNO_3$ sample. Both changes

365 can be associated to the nanoparticles loss during the preparation process, or to a structural
366 incorporation of up to 1% wt. of nanoparticles due to the possible effects of solubility, or to the
367 formation of a new minor phase. These results show the importance of the methodology used to
368 synthetize the nanofluids.

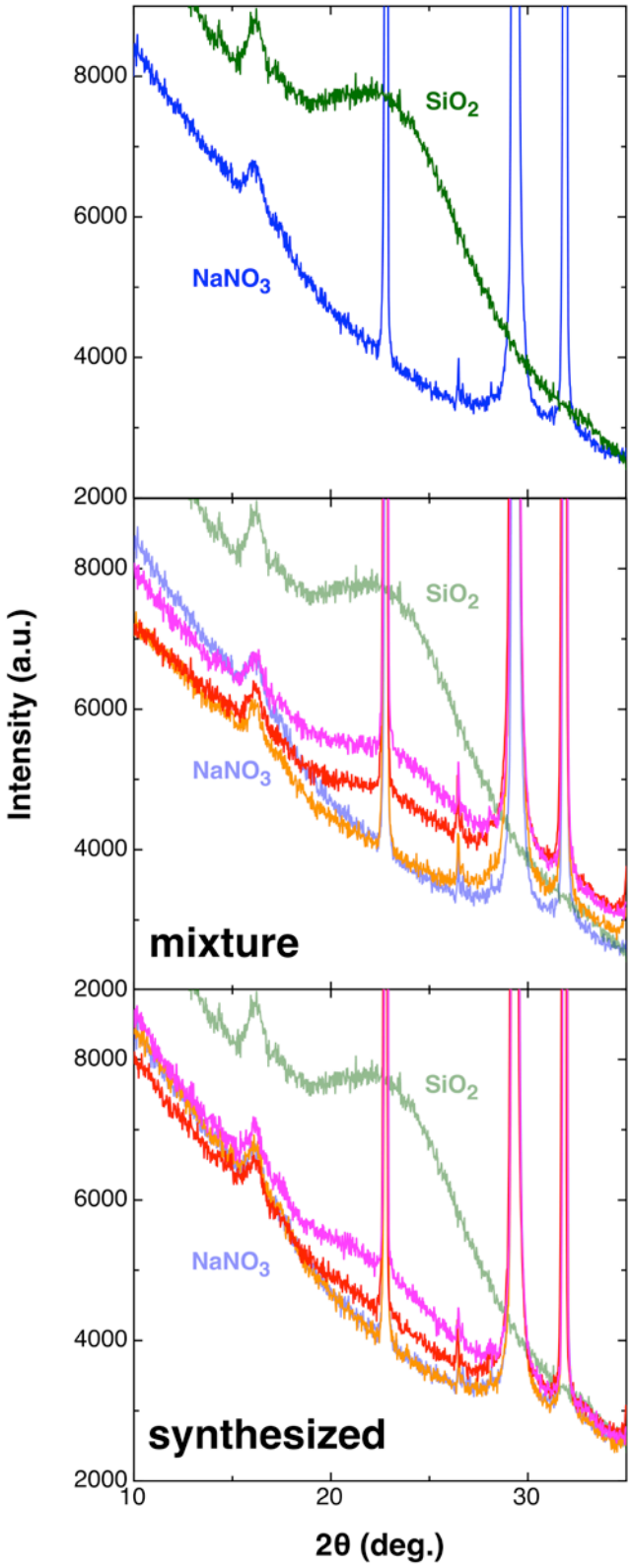

Figure 7. X-Ray Powder Diffraction diagrams in the range 10-35 2θ (°) for SiO_2 nanoparticles (green) and $NaNO_3$ (blue) pure components (top), for the mixtures at different concentrations (middle) and for the synthetized nanofluids (bottom). The nanoparticles concentrations are 1% (orange), 5% (red) and 10% (pink) wt. In the middle and bottom diagrams the SiO_2 and $NaNO_3$ are represented with lower opacity to make comparison easier.

375 The analysis of MD simulations shows the formation of a thin ordered layer around
376 the surface of the nanoparticles at low nanoparticles' concentration. Thus, Figure 8 corresponds
377 to simulation cell snapshots at equilibrium at different temperatures. At 273 K and 300 K, Figure
378 8.a) and 8.b), respectively, $NaNO_3$ is a solid and even so, it is possible to observe the formation
379 of the oriented layer around the nanoparticle surface. When the temperature is increased, the
380 layer's radius grows, as shown in Figure 8.c) at 500K, a temperature close to the phase change
381 of sodium nitrate (*i.e.,* 581 K). Finally, Figure 8.d) shows the system in liquid state at 773 K. At
382 this point, the layer is not evident due to the motion of the fluid. A zoom in the nanoparticle is
383 depicted in Figure 8.e) where a fictional sphere is used to separate the nearest atoms to the
384 surface. It is evident the presence of a higher number of Na^+ cations (yellow spheres) near the
385 surface of the silica nanoparticle as drawn in the scheme of Figure 8.f).
386
387 In order to corroborate this fact, the radial pair distributions have been calculated and
388 plot in Figure 8.g) where the pair distances between the Na^+ cations and the external oxygen
389 atoms of SiO_2 nanoparticles are represented. The formation of a rich semi-solid layer in Na^+
390 cations around the external side of the nanoparticle is observed at a distance between 2.5 Å and
391 3 Å from the surface at all the temperatures explored and with a thickness of approximately 1
392 Å. This fact confirms the existence of the semi-solid layer mechanism at least at 1 nm
393 nanoparticles. Fig. 8.g) also shows the influence of the temperature in the semi-ordered layer.
394 The Na^+ layer density increases as the temperature does, indicating that the layer formation of
395 the liquid molecules in the solid-liquid interface is greater than in the solid state. Dubba et al.,[16]
396 reported the same relation with the temperature that shows opposite results to the ones obtained
397 experimentally in different studies[20,38] who found bigger increments of C_p in solid state.
398
399

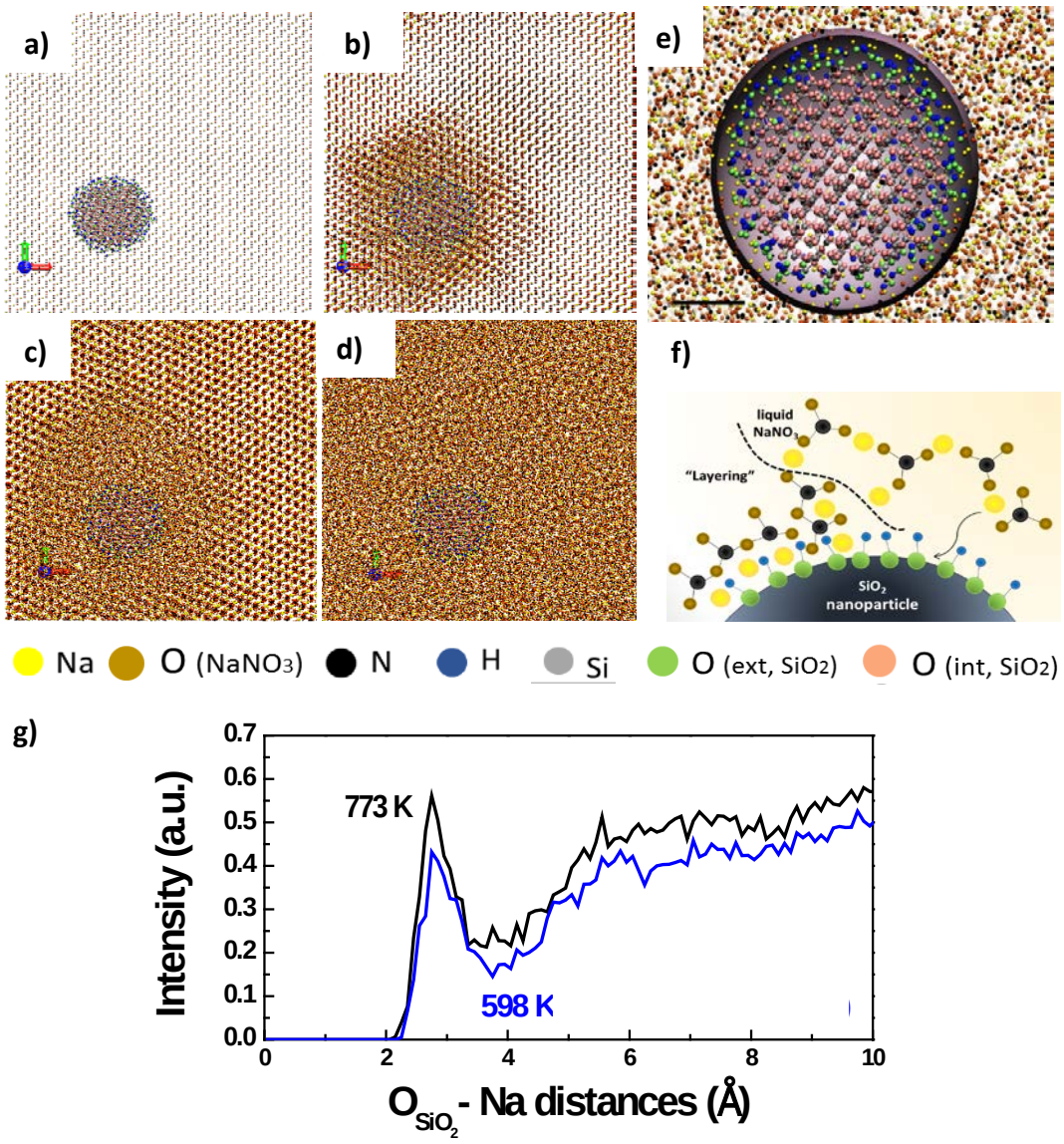

Figure 8. MD snapshots of $NaNO_3$ and SiO_2 nanoparticles of 1 nm of diameter at different temperatures: a) 273 K, b) 300 K, c) 500 K and d) 773 K. e) Expanded snapshot at 773 K for the visualization of the $NaNO_3$ layer near the nanoparticle surface, f) representation of the nanoparticle surface and g) radial pair distribution of Na-O atoms (O from the nanoparticle surface) at 598 K and 773 K.

These results agree with the computational results of Xue et al.,[26] who observed that the magnitude of the layering increases when the solid-liquid interaction strength increases, and results of Hu et al.,[49] or Engelmann et al.,[50] who obtained computationally the same trends for a different ionic system. They concluded that the ordering of the liquid layers is one possible mechanism to counterbalance the Kapitza resistance (interfacial thermal resistance). Also, Shin

et al.,[6] observed via SEM that the alkali salt material apparently has a higher density close to the nanoparticles. This fact also agrees with the layering phenomena observed computationally in Figure 8.

4. Conclusions

The results shown in this study proves the existence of a limit nanoparticles concentration around 2 % wt. for the C_p improvement of the $NaNO_3$ based nanofluid. Therefore, there is a range of concentrations between [0.2 – 2] % wt. where a C_p increment is obtained but the maximum increment is observed around 0.5 – 1 % wt. nanoparticles concentration. The computational results show the same trend than the experimental values obtained by DSC measurements with nanoparticles of 5-15 nm diameters.

Thereafter, the C_p values decrease until reaching the theoretical values of the mixture law when the nanoparticle concentration is higher than 2% wt. This fact is more promising because of the great discrepancy denoted in previous studies between the computational and experimental results or between different studies under the same experimental conditions, showing clear tendencies of the unconventional C_p increment phenomenon.

On the other hand, SEM images indicate nanoparticles agglomerations, and the agglomeration is emphasized when the nanoparticles concentration is higher than 5 % wt. This result matches with the decrease detected of the C_p values.

Moreover, analysis of the radial pair distribution shows the formation of a layer on the nanoparticles surface. This fact approaches the idea of describing the unconventional phenomenon and performance of the C_p. Therefore, the semi-solid layering mechanism is observed in MD simulation.

In summary, based on the results made known in this study the main mechanism to explain the unconventional C_p increment is the Mechanism III previously described: the layering of the liquid molecules around the nanoparticles surface. However, this phenomenon described

448 computationally needs to be verified experimentally and therefore, deep information will be
449 required from properties analysis.

450

451 ## Acknowledgements

452 The research leading to these results is partially funded by the Spanish government
453 RTI2018-093849-B-C32, RTI2018-094757-B-I00, MDM-2017-0767, MCIU/AEI/FEDER,
454 UE). The authors would like to thank the Catalan Government for the quality accreditation given
455 to their research groups DIOPMA (2017 SGR 188) and CMSL (2017 SGR 13). A.S thanks to
456 Generalitat de Catalunya for her Grant FI-DGR 2018, and G.A. acknowledges Universitat de
457 Barcelona for his Grant APIF 2016. Finally, P.G. thanks Generalitat de Catalunya for his Serra
458 Húnter Associate Professorship.

459

460

461

References

1. Desideri, U. & Campana, P. E. Analysis and comparison between a concentrating solar and a photovoltaic power plant. *Appl. Energy* **113**, 422–433 (2014).
2. Hou, Y., Vidu, R. & Stroeve, P. Solar Energy Storage Methods. *Ind. Eng. Chem. Res.* **50**, 8954–8964 (2011).
3. Bauer, T. *et al. High-Temperature Molten Salts for Solar Power Application. Molten Salts Chemistry* (Elsevier Inc., 2013). doi:10.1016/B978-0-12-398538-5.00020-2
4. Bradshaw, R. W. & Siegel, N. P. Molten Nitrate Salt Development For Thermal Energy Storage In Parabolic Trough Solar Power Systems. *Proc. 2nd Int. Conf. Energy Sustain.* 631–637 (2008). doi:10.1115/ES2008-54174
5. Alashkar, A. & Gadalla, M. Thermo-economic analysis of an integrated solar power generation system using nanofluids. *Appl. Energy* **191**, 469–491 (2017).
6. Shin, D. & Banerjee, D. Enhancement of specific heat capacity of high-temperature silica-nanofluids synthesized in alkali chloride salt eutectics for solar thermal-energy storage applications. *Int. J. Heat Mass Transf.* **54**, 1064–1070 (2011).
7. Ahmed, S. F., Khalid, M., Rashmi, W., Chan, A. & Shahbaz, K. Recent progress in solar thermal energy storage using nanomaterials. *Renew. Sustain. Energy Rev.* **67**, 450–460 (2017).
8. Awad, A., Navarro, H., Ding, Y. & Wen, D. Thermal-physical properties of nanoparticle-seeded nitrate molten salts. *Renew. Energy* **120**, 275–288 (2018).
9. Janz, G., Allen, C., Bansal, N., Murphy, R. & Tomkins, R. *Physical properties data compilations relevant to energy storage*.
10. Myers, P. D., Alam, T. E., Kamal, R., Goswami, D. Y. & Stefanakos, E. Nitrate salts doped with CuO nanoparticles for thermal energy storage with improved heat transfer. *Appl. Energy* **165**, 225–233 (2016).
11. Serrano-López, R., Fradera, J. & Cuesta-López, S. Molten salts database for energy applications. *Chem. Eng. Process.* (2013). doi:10.1016/j.cep.2013.07.008
12. Angayarkanni, S. A. & Philip, J. Review on thermal properties of nanofluids: Recent developments. *Adv. Colloid Interface Sci.* **225**, 146–176 (2015).
13. Khanafer, K., Tavakkoli, F., Vafai, K. & AlAmiri, A. A critical investigation of the anomalous behavior of molten salt-based nanofluids. *Int. Commun. Heat Mass Transf.* **69**, 51–58 (2015).
14. Mahian, O., Kianifar, A., Kalogirou, S. A., Pop, I. & Wongwises, S. A review of the applications of nanofluids in solar energy. *Int. J. Heat Mass Transf.* **57**, 582–594 (2013).
15. Wei, X. *et al.* Preparation and enhanced thermal conductivity of molten salt nanofluids with nearly unaltered viscosity. *Renew. Energy* **145**, 2435–2444 (2020).
16. Dudda, B. & Shin, D. Effect of nanoparticle dispersion on specific heat capacity of a

binary nitrate salt eutectic for concentrated solar power applications. *Int. J. Therm. Sci.* **69**, 37–42 (2013).

17. Lu, M.-C. & Huang, C.-H. Specific heat capacity of molten salt-based alumina nanofluid. *Nanoscale Res. Lett.* **8**, 292 (2013).

18. Chieruzzi, M., Miliozzi, A., Crescenzi, T., Torre, L. & Kenny, J. M. A New Phase Change Material Based on Potassium Nitrate with Silica and Alumina Nanoparticles for Thermal Energy Storage. *Nanoscale Res Lett* **10**, 984 (2015).

19. Madathil, P. K. *et al.* Preparation and characterization of molten salt based nanothermic fluids with enhanced thermal properties for solar thermal applications. *Appl. Therm. Eng.* **109**, 901–905 (2016).

20. Luo, Y., Du, X., Awad, A. & Wen, D. Thermal energy storage enhancement of a binary molten salt via in-situ produced nanoparticles. *Int. J. Heat Mass Transf.* **104**, 658–664 (2017).

21. Tiznobaik, H. & Shin, D. Enhanced specific heat capacity of high-temperature molten salt-based nanofluids. *Int. J. Heat Mass Transf.* **57**, 542–548 (2013).

22. Li, Y. *et al.* Experimental study on the effect of SiO 2 nanoparticle dispersion on the thermophysical properties of binary nitrate molten salt. *Sol. Energy* **183**, 776–781 (2019).

23. Hu, Y., He, Y., Gao, H. & Zhang, Z. Forced convective heat transfer characteristics of solar salt-based SiO2 nanofluids in solar energy applications. *Appl. Therm. Eng.* **155**, 650–659 (2019).

24. Qiao, G., Lasfargues, M., Alexiadis, A. & Ding, Y. Simulation and experimental study of the specific heat capacity of molten salt based nanofluids. *Appl. Therm. Eng.* **111**, 1517–1522 (2016).

25. Lan, W., Tan, Z., Meng, S., Liang, D. & Guanghai, L. Enhancement of molar heat capacity of nanostructured Al2O3. *J. Nanoparticle Res. 3* **3**, 483–487 (2011).

26. Xue, L., Keblinski, P., Phillpot, S. R., Choi, S. U. S. & Eastman, J. A. Effect of liquid layering at the liquid-solid interface on thermal transport. *Int. J. Heat Mass Transf.* **47**, 4277–4284 (2004).

27. Li, L., Zhang, Y., Ma, H. & Yang, M. Molecular dynamics simulation of effect of liquid layering around the nanoparticle on the enhanced thermal conductivity of nanofluids. *J. Nanoparticle Res.* **12**, 811–821 (2010).

28. Plimpton, S. Fast Parallel Algorithms for Short – Range Molecular Dynamics. *J. Comput. Phys.* **117**, 1–19 (1995).

29. Schneider, T. & Stoll, E. Molecular-dynamics study of a three-dimensional one-component model for distortive phase transitions. *Phys. Rev. B - Condens. Matter Mater. Phys.* **17**, (1978).

30. Berendsen, H. J. C. *et al*. Molecular dynamics with coupling to an external bath. *J. Chem. Phys.* **3684**, (1984).
31. Martyna, G. J., Tobias, D. J. & Klein, M. L. Constant pressure molecular dynamics algorithms. *J. Chem. Phys.* **101**, 4177–4189 (1994).
32. Parrinello, M. & Rahman, A. Polymorphic transitions in single crystals : A new molecular dynamics method Polymorphic. *J. Appl. Phys.* **7182**, (2012).
33. Sun, H. COMPASS: An ab Initio Force-Field Optimized for Condensed-Phase Applications s Overview with Details on Alkane and Benzene Compounds. *J. Phys. Chem. B* **5647**, 7338–7364 (1998).
34. Hockney, R. W. & Eastwood, J. W. *Computer simulation using particles*. (McGraw-Hill International Book Co., c1981., 1989).
35. Jayaraman, S., Thompson, A. P., von Lilienfeld, O. A. & Maginn, E. J. Molecular Simulation of the Thermal and Transport Properties of Three Alkali Nitrate Salts. *Ind. Eng. Chem. Res.* **49**, 559–571 (2010).
36. Patwardhan, S. V *et al*. Chemistry of Aqueous Silica Nanoparticle Surfaces and the Mechanism of Selective Peptide Adsorption. (2012). doi:10.1021/ja211307u
37. Khanafer, K., Tavakkoli, F., Vafai, K. & AlAmiri, A. A critical investigation of the anomalous behavior of molten salt-based nanofluids. *Int. Commun. Heat Mass Transf.* **69**, 51–58 (2015).
38. Chieruzzi, M., Cerritelli, G. F., Miliozzi, A. & Kenny, J. M. Effect of nanoparticles on heat capacity of nanofluids based on molten salts as PCM for thermal energy storage. *Nanoscale Res. Lett.* **8**, 448 (2013).
39. Takahashi, Y., Sakamoto, R. & Kamimoto, M. Heat capacities and latent heats of LiNO3, NaNO3, and KNO3. *Int. J. Thermophys.* **9**, 1081–1090 (1988).
40. Bauer, T., Laing, D. & Tamme, R. Characterization of sodium nitrate as phase change material. *Int. J. Thermophys.* **33**, 91–104 (2012).
41. Ichikawa, K. & Matsumoto, T. Heat Capacities of Lithium, Sodium, Potassium, Rubidium, and Caesium Nitrates in the Solid and Liquid States. *Bulletin of the Chemical Society of Japan* **56**, 2093–2100 (1983).
42. Ferrer, G., Barreneche, C., Solé, A., Martorell, I. & Cabeza, L. F. New proposed methodology for specific heat capacity determination of materials for thermal energy storage (TES) by DSC. *J. Energy Storage* **11**, 1–6 (2017).
43. Sridhara, V. & Satapathy, L. N. Al2o3-based nanofluids: A review. *Nanoscale Res. Lett.* **6**, 1–16 (2011).
44. Philip, J. & Shima, P. D. Thermal properties of nanofluids. *Adv. Colloid Interface Sci.* **183**–**184**, 30–45 (2012).
45. Rashmi, W., Khalid, M., Ong, S. S. & Saidur, R. Preparation, thermo-physical properties

and heat transfer enhancement of nanofluids. *Mater. Res. Express* **1**, (2014).

46. Xie, Q., Zhu, Q. & Li, Y. Thermal Storage Properties of Molten Nitrate Salt-Based Nanofluids with Graphene Nanoplatelets. *Nanoscale Res. Lett.* **11**, 306 (2016).

47. Jriri, T., Rogez, J., Bergman, C. & Mathieu, J. C. Thermodynamic study of the condensed phases of NaNO3, KNO3 and CsNO3 and their transitions. *Thermochim. Acta* **266**, 147–161 (1995).

48. Wang, B.-X., Zhou, L.-P. & Peng, X.-F. Surface and Size Effects on the Specific Heat Capacity of Nanoparticles. *Int. J. Thermophys.* **27**, 139–151 (2006).

49. Hu, Y., He, Y., Zhang, Z. & Wen, D. Enhanced heat capacity of binary nitrate eutectic salt-silica nanofluid for solar energy storage. *Sol. Energy Mater. Sol. Cells* **192**, 94–102 (2019).

50. Engelmann, S. & Hentschke, R. Specific heat capacity enhancement studied in silica doped potassium nitrate via molecular dynamics simulation. *Sci. Rep.* **9**, 1–14 (2019).